The Role of Inhomogeneities for Understanding Current–Voltage Characteristics of Solar Cells

Otwin Breitenstein

Abstract—All solar cells show more or less inhomogeneous electronic properties. This holds in particular for multicrystalline silicon cells, where local differences of the lifetime of more than an order of magnitude exist. This contribution explains how these inhomogeneities can be imaged and quantified, and the physical origins and the efficiency degradation potential of J_{01}-, J_{02}-, and ohmic inhomogeneities are reviewed. It is found that J_{02} and ohmic currents are always highly localized, in contrast with J_{01} currents. Hence, for describing most of the area of silicon solar cells, a one-diode model is sufficient, but J_{02} and ohmic currents reduce the efficiency at low illumination intensity. Moreover, the physical origins of known prebreakdown phenomena are reviewed and a new breakdown type dominating in monocrystalline silicon cells is proposed.

Index Terms—Breakdown mechanisms, crystalline silicon cells, dark current analysis, efficiency analysis, inhomogeneities, lock-in thermography (LIT).

I. Introduction

IN 2016, more than 69% of all installed solar modules still were made from multicrystalline (mc) silicon material, monocrystalline is only slowly catching up [1]. Even in most advanced high-performance (HP) mc material showing best lifetimes above 1 ms, defect regions exist showing local lifetimes well below 100 μs [2]. Though the areal fraction of these defect regions is reduced in HP mc material, they still limit the efficiency of PERC cells, as will be shown below. Therefore, studying and evaluating the influence of low-lifetime regions on the efficiency remains important. Moreover, the dark characteristics of most solar cells indicate in the low-voltage region the presence of an ohmic parallel resistance R_p and of depletion region recombination, which is described in the two-diode model by the saturation current density J_{02} and an ideality factor n_2, usually measured to be larger than 2. These leakage currents influence the efficiency [in particular the fill factor (FF)] even of good solar cells, in particular under reduced illumination intensity, as will be shown below. For optimizing the FF and the low light level performance of solar cells, also these leakage current phenomena have to be characterized and understood.

In this paper, the first experimental methods for characterizing electronic inhomogeneities in solar cells and predicting their influence on the cell efficiency are reviewed with special consideration of dark lock-in thermography (DLIT). Then, mainly based on our work in the last 20 years, the physical origins of locally increased J_{01}, J_{02}, and ohmic currents will be identified. On typical standard technology and PERC cells on mc Si material the influence of these three loss mechanisms on the cell efficiency will be estimated for different illumination intensities. Finally, the physical origins of prebreakdown phenomena in mc silicon solar cells will be reviewed and some new findings regarding prebreakdown in monocrystalline cells are presented.

II. Solar Cell Imaging Methods

The three most important methods for imaging electronic parameters of solar cells are monochromatic light beam-induced current (LBIC) mapping, lock-in thermography (LIT), and luminescence imaging, see e.g., [3]. LBIC mapping at various wavelengths allows to image the short-circuit current density J_{sc} for AM 1.5 realistically [4] and, if combined with reflectivity measurement, the monochromatic internal quantum efficiency. The choice of the excitation wavelength governs the mean excitation depth, which allows to image the effective diffusion length L_{eff}, and with this the bulk saturation current density J_{01} [5]. Note that in the calculation of L_{eff} some optical properties of the surface texture go in, which may lead to certain errors if not correctly assumed. This may lead to certain discrepancies between LBIC- and LIT-based J_{01} images. Multispectral LBIC systems are not very widespread, there seem to be only a few commercial vendors [6]. Physically, LBIC is similar to the electron beam-induced current (EBIC) imaging technique, which shows a better spatial resolution but lower information depth, see [3].

The second solar cell imaging method, which, since its introduction in 2000, has become a widespread standard method for characterizing solar cells, is LIT [7]. There are many variants of this technique. In its most popular variant dark LIT (DLIT), a pulsed forward or reverse bias is applied to the cell and the local surface temperature modulation, measured by an IR thermocamera, is a measure of the local dark current density. In the "Local I–V" method [8], the software of which is available [9], up to four DLIT images taken at different biases are used for fitting each image pixel to a two-diode model, leading to images of the saturation current densities of the first and the second diode J_{01} and J_{02}, the ideality factor of the second diode n_2, and the ohmic parallel conductivity $G_p = 1/R_p$. The ideality factor of the first diode n_1 is allowed to be chosen larger than unity for considering an injection intensity-dependent lifetime,

This article has been accepted for inclusion in a future issue of this journal. Content is final as presented, with the exception of pagination.

2   IEEE JOURNAL OF PHOTOVOLTAICS

see Section III-A, but this ideality factor is assumed to hold globally. The local short-circuit current density J_{sc} can be assumed to be homogeneous, an image of J_{sc} can be loaded, or J_{sc} can be simulated from the obtained J_{01} distribution after [10]. The effective local series resistance R_s can be assumed to be homogeneous, an image of R_s can be loaded, or it can be simulated from an EL-based image of the local diode voltage at the highest used forward bias after [11]. Until now "Local I-V" is the only method that can reliably distinguish these three dark current components and evaluate them quantitatively. Knowing these local two-diode parameters allows "Local I-V" to simulate local and global illumination intensity-dependent efficiency parameters, like potential values of V_{oc}, the FF, and the efficiency η [12]. As a rule, the globally simulated efficiency matches the measured one of the cell well. By selecting certain regions for the efficiency analysis (e.g., the best region in a cell or the cell without the edge region) the influence of all defect regions in a cell or of the edge region on the efficiency can be quantified. The "cut shunt" option, where the properties in a selected shunt region are replaced by that of the surrounding, allows to predict the global cell efficiency without the influence of certain local defects.

The youngest and meanwhile the most widespread solar cell imaging technique is luminescence imaging, for an overview, see [13]. The simplest variant is electroluminescence (EL) imaging, where just a forward bias is applied and the luminescence is imaged with a sensitive (often cooled) Si charge-coupled device camera. Also reverse-bias EL (ReBEL) can be performed, here the luminescence mechanism is completely different to that under forward bias [14]. For photoluminescence (PL) imaging, the cell is illuminated homogeneously and the illumination light has to be removed by placing an appropriate filter in front of the camera. EL imaging is used widespread for qualitatively detecting local recombination centers, cracks, and high-R_s regions, both in cells and in modules. PL imaging performed under current load enables reliable quantitative R_s imaging [13], [15]. Earlier attempts to image also J_{01} and J_{02} by EL or PL have been found to be erroneous [16], but meanwhile alternative methods for high-resolution J_{01} imaging by PL are available [3].

III. Origin and Influence of Inhomogeneities

In this section, the dominant origins of inhomogeneities of J_{01}, J_{02}, and $G_p = 1/R_p$ in mc solar cells will be reviewed and illustrated on some examples. In the discussion of the images the influence of certain defect regions on the global efficiency of the cell will be determined, based on the 'Local I-V' analysis of the corresponding cells. The images shown here belong to standard technology (BSF type) cells, but the same efficiency analysis was performed also to a PERC cell produced from HP p-type mc Si material, which was kindly provided by Trina Solar, Changzhou. The "Local I-V"-based simulation results of the quantitative influence of defect regions will be given both for the investigated BSF cells and for the PERC cell. Finally also prebreakdown mechanisms will be reviewed and a new
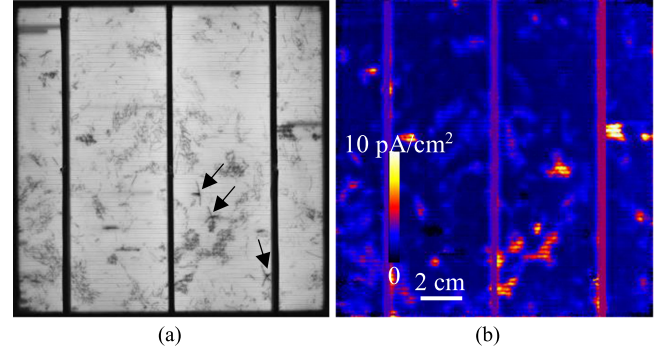

Fig. 1. (a) EL image [a.u.], arrows point to cracks. (b) DLIT-based J_{01} image of a standard technology mc Si cell.

breakdown mechanism dominating in monocrystalline cells will be proposed.

A. J_{01} Inhomogeneity

The dominant sources of J_{01} inhomogeneities in mc cells are that of the bulk lifetime caused by grown-in crystal defects and the inhomogeneity of the backside recombination velocity [2]. It is well known that injection-dependent lifetimes may lead to ideality factors of J_{01} larger than one [17], [18]. This increase of the ideality factor can be regarded in "Local I-V" by assuming $n_1 > 1$ homogeneously and has not to be confused with J_{02} effects, which exist in parallel, see Section III-B. Fig. 1 shows an EL image of a standard technology mc solar cell together with a J_{01} image of this cell obtained by evaluating DLIT images after the "Local I-V" method [8].

We see in the EL image in Fig. 1(a) a network of fine dark lines, which are concentrated in groups. These groups are the so-called defect regions, sometimes also called dislocation tangles, which until now cannot be completely avoided in mc material but only minimized. The dark lines are recombination-active grain boundaries (GBs), the strongest ones typically being low-angle GBs. It has been found by high-resolution scanning transmission electron microscopy (STEM) that their recombination activity depends on their content of a special type of dislocations [19]. The most useful imaging mode for imaging rows of single atoms in a high-resolution STEM is low-angle annular dark field (LAADF), which images single atom rows as bright spots. Elastic strain leads in this imaging mode to bright regions. This is demonstrated in Fig. 2(a) showing an LAADF image taken with an FEI TITAN 80-300 STEM implying probe C_s-correction [19]. Here, on two curved small-angle grain boundaries (SAGBs) showing inhomogeneous recombination activity, in six positions showing different recombination activities (measured by EBIC), TEM specimens were prepared. In these SAGBs obviously the recombination activity depended on the orientation of the GB with respect to the lattice orientation, which is observed regularly. This orientation leads to different types of the dislocations yielding the SAGBs. Then, by LAADF STEM the types of the dislocations yielding the SAGB were identified in each sample position. Most of the dislocations are split into partials with stacking faults in between, as usual for
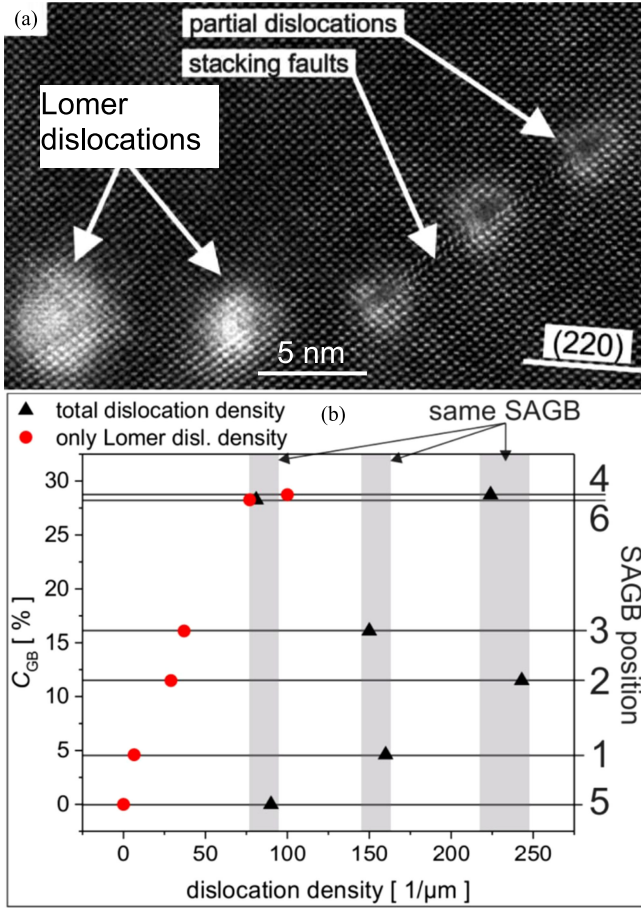
Fig. 2. (a) LAADF STEM image of a recombination-active SAGB. (b) Dependence of the EBIC contrast on the total dislocation density in the GB (black triangles) and on the density of Lomer dislocations (red dots).

Fig. 3. (a) Forward bias and (b) reverse bias characteristics for virgin, cleaved, laser cut, and scratched PERL cells.

dislocations in Si. However, some of them are a special type of edge dislocations, identified by their Burgers vector as perfect (nonsplit) Lomer dislocations [20], which are known to be quite immobile. The strain field of the Lomer dislocations in Fig. 2 is significantly higher than that of the partial dislocations. Fig. 2(b) shows, for the six positions in two SAGBs, the EBIC contrast of the GB $C_{GB}[\%]$ as a function of the total dislocation density per μm and of the Lomer dislocation density. We see that the EBIC contrast only correlates with the density of Lomer dislocations, but not with the total dislocation density. This proves that the Lomer dislocations are dominating the recombination activity of these SAGBs and probably also generally in the mc Si material. The reason for their recombination activity is probably their immobile and nonsplit character and their higher strain field, which prefers iron contamination there in the process of crystal cooling.

We also see in the EL image in Fig. 1(a) some cracks (see arrows) and some dark regions of increased R_s due to broken gridlines, e.g., in the upper left corner. The "Local I-V"-based J_{01} image in Fig. 1(b) does not show these cracks and high $-R_s$ regions, but it shows the defect regions in (a) as local J_{01} maxima, the strongest ones approaching 17 pA/cm^2. The mean value of J_{01} is 1.7 pA/cm^2, in the defect-free regions J_{01} is as low as 1 pA/cm^2. The "Local I-V" cell simulation [12] reveals that the whole cell is characterized by $V_{oc} = 618$ mV and
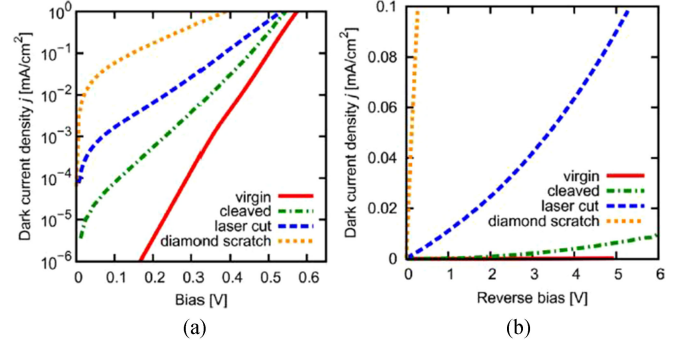
$\eta = 16.2\%$, in good agreement with measured values, whereas the best regions show potential values of $V_{oc} = 633$ mV and $\eta = 17.0\%$. Hence, the defect regions reduce V_{oc} significantly by 15 mV and η by 0.8% (absolute). The amount of this reduction is only little dependent on the illumination intensity. The cracks are not visible in the J_{01} image (b), since they express in the J_{02} current, see next subsection III-B. In the also investigated mc PERC cell (images not shown here), the global J_{01} was found to be 288 fA/cm^2, the minimum J_{01} was 154 fA/cm^2, and the maximum J_{01} was 3 pA/cm^2, which is clearly less than for the standard technology cell. In the PERC cell the defect regions reduced V_{oc} by 21 mV and η by 1.1% (absolute). Hence, though this cell was made from HP material containing less defect regions by area and a lower defect-induced maximum J_{01}, the influence of the defect regions was even larger than in the standard technology cell. This is due to the significantly lower J_{01} in the good regions of this cell. For both cells the defects reduce mainly V_{oc} and thus V_{mpp} by increasing J_{01}, and this reduction is only weakly dependent on the illumination intensity.

B. J_{02} Inhomogeneity

Already in 1994 we have found by successively dividing a solar cell into smaller pieces and comparing the dark current density characteristics that the cell edge leads to a dark current contribution with a high ideality factor [18], [21]. Decisive progress in understanding the physics of J_{02}-type shunts has been made by investigating the influence of cleaves or surface scratches made on flat laboratory PERL cells produced by planar technology with their cell edge passivated by a field oxide [22], [23]. In virgin state, these cells show an ideal I–V characteristic with an ideality factor close to 1 over a large bias range. As soon as the cells are cleaved or scratched at the surface, their characteristic converts into that common for industrial solar cells, showing in the low bias range a large J_{02} current with an ideality factor n_2 of or larger than 2. As can be seen in Fig. 3(a), the cleaved cell shows the lowest ideality factor, the laser cut a medium one, and the diamond scratched cell shows the largest ideality factor. Similar differences occur by diamond scratching with increasing loads [18], [22]. Under reverse bias (b) the virgin cell shows a negligible and the other cells an increasingly stronger ohmic reverse current, partly including some superlinear (prebreakdown) behavior. This will be discussed further in Section III-D. All these phenomena can be explained by
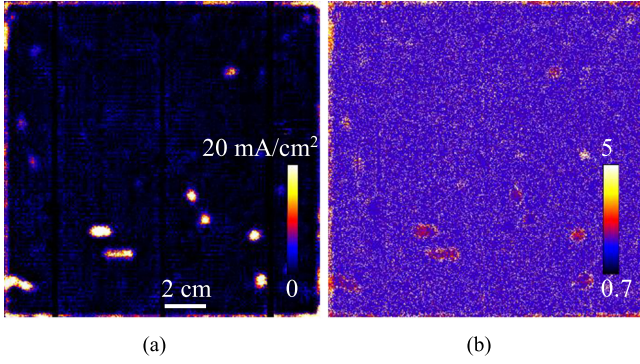
Fig. 4. (a) Depletion region recombination current density at 600 mV bias of the cell of Fig. 1. (b) n_2 image.
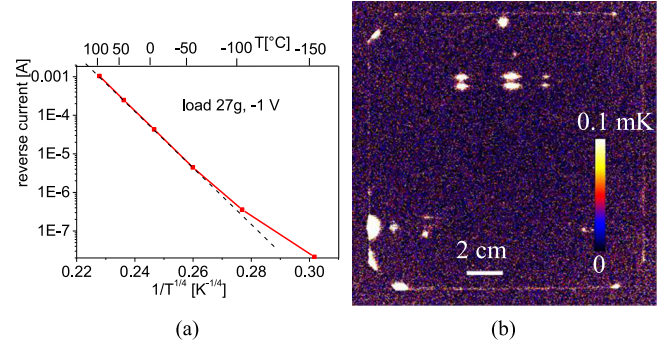

Fig. 5. (a) Temperature dependence of the reverse bias leakage current at -1 V caused by a scratch in a previously leakage-free cell. (b) Reverse-bias DLIT image at -1 V of an industrial monocrystalline standard technology cell.

extended defects crossing the p-n junction, which lead, due to their very high local density of recombination states, to overlapping of the defect wave functions and thus to multilevel recombination beyond the Shockley–Read–Hall approximation. In fact, the J_{02} current is negligibly small in most of the areas (also in defect regions [18]) and is strongly localized in some positions, e.g., at scratches or in the edge region. This is a proof of the nature of the J_{02} current found already in [21] and [22] and confirmed by Sentaurus device simulations in [23]: Yes, the J_{02} current is due to depletion region recombination. However, the homogeneous (bulk lifetime-governed) J_{02} current as predicted by Sah–Noice–Shockley with $n_2 = 2$ is negligibly small for Si solar cells [18]. The dominant contribution to J_{02} is caused by extended defects crossing the depletion region, like the non-passivated surface in edge regions or scratches through the p-n junction. In these extended defects the local defect state concentration is so high that multilevel recombination becomes probable, which leads to the observed high ideality factors [22], [23].

If, as in the case of the cell shown in Fig. 1, the ideality factor of the second diode n_2 is taken in the "Local I-V" analysis as a variable, it is not useful to display the saturation current density J_{02}, since it is not proportional to the J_{02}-type current anymore [12]. Instead, it is useful to display the simulated depletion region recombination current density at a certain voltage as done in Fig. 4(a). Alternatively, "Local I-V" allows to assume $n_2 = 2$, leading to a J_{02} image that is widely equivalent to Fig. 4(a). Then only the device modeling for low currents is not as perfect anymore. The comparison between Figs. 4(a) and 1(b) shows that the J_{01}- and J_{02}-type currents are completely differently distributed and can be reliably separated from each other by applying the "Local I-V" method to DLIT images. The scaling range of the DLIT-measured ideality factor (n_2) image in Fig. 4(b) chosen as $n_2 = 2$ corresponds to blue color. We see that nearly all local J_{02} currents show a higher ideality factor than 2, reaching values close to $n_2 = 5$ in the upper left corner edge. The cracks indicated in Fig. 1(a) by arrows cause strong J_{02} currents in Fig. 4(a). The horizontal stripes of J_{02} current in the lower cell part, which are also visible in Fig. 1(a) due to their local current-induced voltage drop, are surface scratches. The "Local I-V" evaluation has revealed that the edge J_{02} shunts visible in Fig. 4(a) reduce at 1 sun the FF by 0.5%, η by 0.1% (absolute), and $V_{\rm oc}$ not measurably, but at 0.1 suns they reduce the FF by

1.3%, η by 0.3% (absolute), and $V_{\rm oc}$ by 2 mV. This shows that, in contrast with the defect-induced J_{01} currents, the J_{02} currents generated by extended defects crossing the p-n junction degrade the efficiency at low illumination intensity considerably more than at full illumination intensity. For the PERC cell the edge region reduces at 1 sun the FF by 0.6%, η by 0.1%, and $V_{\rm oc}$ by 1 mV, whereas at 0.1 sun it reduces the FF by 1.3%, η by 0.3%, and $V_{\rm oc}$ by 3 mV. These data are similar to that of the BSF cell.

C. Ohmic Shunts

In the analysis of dark currents even of well-processed silicon solar cells, as a rule a weak ohmic conductivity is detected under reverse bias. In the traditional two-diode model, ohmic conductivity is assumed to be evenly distributed across a solar cell. However, there is no physical explanation for a homogeneous ohmic conductivity in Si solar cells. DLIT is the method of choice to image even weak ohmic shunts. Indeed, it has been found very early that ohmic shunts in Si solar cells are always local phenomena [18], [24]. In mc and monocrystalline Si cells, ohmic shunts may be due to extended defects crossing the p-n junction, just like the J_{02}-type currents. If the local defect level density in these defects is high enough, tunneling currents may flow across these levels leading to variable range hopping conduction according to Mott's theory [25]. This has been proven by measuring the $\log(I)$ versus $1/(T)^{1/4}$ temperature dependence of the ohmic leakage current caused by surface scratching shown in Fig. 5(a) [22]. The same type of reverse current is visible at the edges of solar cells as shown in the DLIT image of a monocrystalline cell at -1 V shown in Fig. 5(b). Note that the reverse current at the edge of this cell is extremely weak, as can be seen from the scaling range and by the presence of noise in spite of the long acquisition time of several hours.

Other obvious causes of ohmic shunts are an incompletely opened emitter at the cell edge, cracks (containing the emitter or filled with metal paste), and Al particles at the surface [18], [24]. The latter diffuse-in during contact firing and cause local p^+ regions around, which are in direct contact to the p-type base and yield an ohmic tunnel contact to the emitter, see also Section III-D.

Potential-induced degradation also leads to local ohmic shunts and to additional J_{02} currents with a high ideality factor [26].
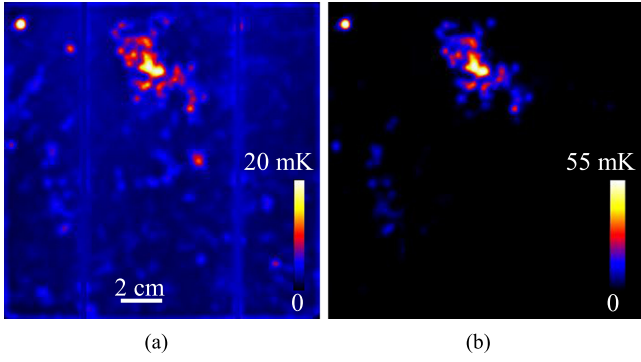
This article has been accepted for inclusion in a future issue of this journal. Content is final as presented, with the exception of pagination.

BREITENSTEIN: ROLE OF INHOMOGENEITIES FOR UNDERSTANDING CURRENT–VOLTAGE CHARACTERISTICS OF SOLAR CELLS 5

(a) (b)

Fig. 6. (a) DLIT image of a shunted cell taken at $+600$ mV. (b) DLIT image at -1 V.

(a) (b)

Fig. 7. (a) Superposition of forward bias EL and ReBEL image. (b) ReBEL signal of single type 2 breakdown sites as a function of reverse voltage.

Highly sensitive EDX analyses have revealed that in these positions planar defects on $<111>$ planes exist, looking similar to stacking faults, which contain Na. It is assumed that the ohmic and J_{02} conduction mechanisms of these defects are similar to that of the above discussed extended defects crossing the p-n junction, namely hopping conduction between neighboring defect levels and multilevel recombination [26].

The most disturbing ohmic shunts in mc cells are caused by SiC filaments crossing the cell. In the vertical crystallization fabrication of mc material, carbon may enrich in the upper part of the block and may lead to SiC precipitates, which usually appear in form of vertically growing filaments, some μm in diameter and some mm in length [27]. These SiC filaments are highly n-conducting by N doping and may short circuit the cell from the emitter to the back contact [28].

The cell used in Sections III-A and III-B did not show measurable ohmic shunts. Therefore, here results of another mc standard technology cell containing material-induced ohmic shunts (SiC filaments) will be presented [29]. Fig. 6(a) shows a DLIT image of this cell under 0.6 V forward bias and (b) under -1 V reverse bias. All bright spots (shunts) appearing both at forward and reverse bias are ohmic shunts, whereas all signals appearing only at forward bias are J_{01} and J_{02} currents. In a "Local I-V" analysis of this cell, all ohmic shunts have been virtually cut out and replaced by the surrounding properties by using the "cut shunt" option. This procedure has revealed that all ohmic shunts reduce at 1 sun the FF by 3.3%, V_{oc} by 2 mV, and η by 0.8%, and at 0.1 sun the FF by 25.3%, V_{oc} by 22 mV, and η by 5.1% (absolute). This demonstrates that ohmic shunts are degrading the efficiency under reduced illumination intensity even stronger than J_{02}-type shunts. This is due to the fact that, with reducing bias, the leakage current of ohmic shunts drops much less than that of J_{01}- and J_{02}-type shunts.

D. Breakdown Sites

In semiconductor textbooks [30], two breakdown mechanisms for p-n junctions are described, which are avalanche (carrier multiplication) breakdown and internal field emission (tunneling through the gap, Zener breakdown), the latter dominating for high doping densities. Both breakdown mechanisms may show a homogeneous breakdown current in a homogeneous device and are used in semiconductor industry.
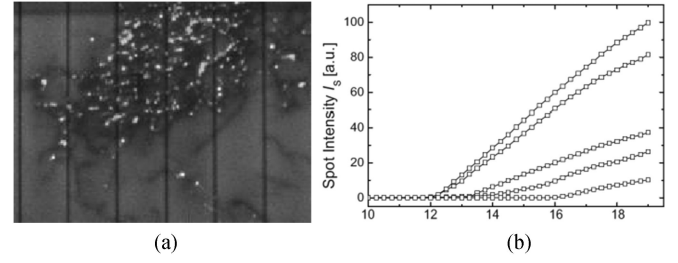
Silicon solar cells with a bulk doping density of 10^{16} cm^{-3} should breakdown homogeneously by avalanche at -60 V [31].

However, in particular for mc cells some prebreakdown may occur already below -10 V, and there are always ohmic currents under reverse bias. By reverse-bias DLIT and ReBEL imaging, systematic investigations of these prebreakdown phenomena in mc silicon solar cells, summarized in [32], have revealed three different breakdown mechanisms in mc cells, which dominate typically in three different voltage ranges. All these breakdown mechanisms are local phenomena, hence they occur at microscopically small breakdown sites. By measuring the temperature dependence of the global breakdown current, it was found that, up to a reverse bias of typically -13 V, the temperature coefficient (TC) of the reverse current is positive, but beyond -13 V it may become negative. The only mechanism showing a negative TC of the current is avalanche breakdown. The question rises how avalanche breakdown, which is expected to occur only at -60 V, may occur at such low voltages.

At low reverse biases below -8 V, and partly being responsible for the ohmic reverse current, we speak of "early breakdown" or "type 1" breakdown. For this breakdown type, a very poor correlation between ReBEL and DLIT has been found [32]. According to Lausch et al. [33], this breakdown type is due to Al particles at the surface. During contact firing these particles alloy-in at the surface and overcompensate the emitter around, leading to an n^+-p^+ junction to the emitter. Depending on the p^+ doping density in this region, this junction may be a Zener diode with a low breakdown voltage or an ohmic tunnel junction. This explains why some of these type 1 breakdown sites show ReBEL and some others do not.

The "defect-induced" (type 2) breakdown dominates for typical mc cells in the bias range between -8 and -12 V and is found only in the typical regions showing recombination-active defects in mc material [32]. This is demonstrated in Fig. 7(a) showing the superposition of an EL image under forward bias, displaying recombination-active GBs as dark lines, and a ReBEL image under -12 V reverse bias (the bright spots). We see that practically all breakdown sites are lying at or close to the GBs.

Schneemann et al. [34] have shown that the breakdown at single type 2 breakdown sites may set on at different voltages, and that the current of all these sites is series resistance-limited. This is demonstrated by the ReBEL intensities of individual type 2 breakdown sites shown in Fig. 7(b). By performing analytical TEM investigations on such a site, we have shown that in these sites α-FeSi$_2$ needles with a diameter of about 20 nm and some μm length are crossing the p-n junction [35]. This
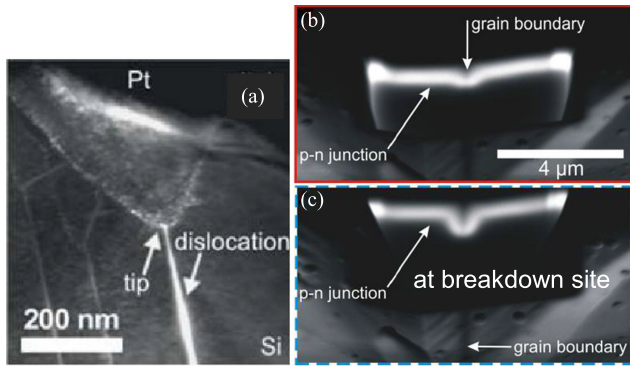
Fig. 8.   (a) TEM image of an etch pit in a mc cell, EBIC images of an FIB cut through the p-n junction at a grain boundary with flat surface. (b) Besides a breakdown site. (c) At a breakdown site.

Fig. 9.   (a) Reverse-bias (–15 V) DLIT image of a monocrystalline cell [a.u.]. (b) 0.5 V forward bias DLIT image of this cell [a.u.].

silicide material is quasi-metallic and yields an ohmic contact to the highly doped emitter and a Schottky contact to the base. Thus, the breakdown mechanism is thermionic field emission, enhanced by the tip effect [32]. The different orientations and positions of the $FeSi_2$ needles in the material lead to the observed different breakdown set-on voltages of the different sites. The small size of the breakdown sites explains their high individual series resistance. In [32], for a 1 μm sized defect in 1 Ωcm material, a series resistance of 3.2 kΩ was estimated.

The third (type 3) breakdown mechanism reported in [32] was identified as avalanche breakdown below etch pits. The acidic etch used for texturization of mc material is actually optimized not to lead to preferred defect etching. However, special types of dislocations nevertheless lead to funnel-shaped etch pits in the surface of mc cells. It has been found by reverse-bias lock-in EBIC that in these positions avalanche multiplication occurs at voltages beyond –13 V [36]. Fig. 8(a) shows a TEM image of the tip of such an etch pit. The p-n junction is lying about 300 nm below the surface. If this surface is a sharp etch pit, the p-n junction below is expected to be of spherical shape with the center at the tip and a radius of about 300 nm. In such a spherical shaped p-n junction the avalanche breakdown voltage for a doping concentration of 10^{16} cm^{-3} is reduced from -60 to -13 V [31]. This is just the onset voltage of the type 3 breakdown and the avalanche multiplication in the investigated cells. Since the spherical radius of the p-n junction below all etch pits is expected to be the same, all these sites show the same breakdown voltage, in contrast with the defect-induced (type 2) breakdown sites, see Fig. 7(b). Therefore, the slope of the local I–V characteristic of the type 3 breakdown sites was measured by reverse-bias DLIT to be steeper than that of the type 2 sites [37]. Another proof of the avalanche type of the type 3 breakdown sites is that only these sites show a negative TC of the current and avalanche amplification of the photocurrent, both measured by special LIT methods [37].

In alkaline etched mc cells, there are no etch pits, but nevertheless avalanche breakdown could be identified, though occurring at higher reverse bias [38]. By performing EBIC on a vertical focused ion beam (FIB) cut through the p-n junction in two positions of a GB, one besides and one at a breakdown site, we have observed preferred phosphorous diffusion in this GB. The surface above these sites was perfectly flat. Besides the
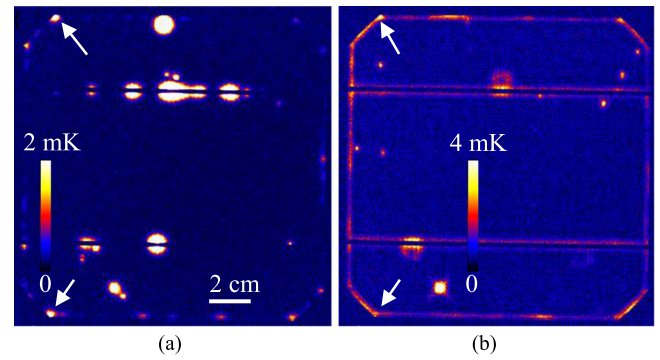
breakdown site, only weak preferential diffusion of P in the GB is observed [see Fig. 8(b)], but it is clearly stronger at the breakdown site (c). Here, TEM investigations revealed a "kink" in the GB, which represents a special line defect leading to preferred P diffusion into the depth. Also, here we expect a spherical-shaped p-n junction, the EBIC-measured sphere radius agreed well with the breakdown voltage measured by micro-ReBEL regarding [31], [38].

From these three prebreakdown mechanisms, only the Al-induced early breakdown (type 1) may occur also in defect-free monocrystalline silicon solar cells, if there are Al particles at the surface. Nevertheless, also in otherwise perfect monocrystalline cells, we find prebreakdown, though at higher reverse biases, and also a residual ohmic reverse conductivity. Fig. 9(a) shows a reverse-bias DLIT image of a monocrystalline standard technology cell taken at –15 V, and (b) shows a forward-bias DLIT image of this cell taken at +0.5 V. At this low forward bias, the image is clearly dominated by J_{02} currents. Since this was an already stressed elder cell [the same as used for Fig. 5(b)], here we find some defects in the area and below the busbars, but the essential result is at the cell edge. We clearly see at +0.5 V (b) the J_{02} edge current, as it was visible for an mc cell also in Fig. 4(a). Note that this J_{02} edge current is, with a DLIT signal of up to 4 mK for 0.5 V bias, about two orders of magnitude stronger than the reverse current of the same cell shown in Fig. 5(b), which showed a DLIT signal in the order of 0.1 mK at –1 V bias. In the positions of maximum J_{02} edge currents [arrows in Fig. 9(b)], we also find prebreakdown at the edge in Fig. 9(a). The mechanism is again conductivity across extended defect states at the nonpassivated surface, but at low voltages it is hopping conduction and at higher voltages probably trap-assisted (here multilevel assisted) tunneling through the gap. Already the measurements shown in Fig. 3(b) pointed to a superlinear (breakdown-type) contribution of the reverse current through extended defects. It can be concluded that the dominating prebreakdown and ohmic reverse conduction mechanism in otherwise perfect monocrystalline silicon solar cells is hopping and multilevel assisted tunneling across surface states in the edge region. The physical nature of this mechanism still should be further investigated, e.g., by measuring its temperature dependence and comparing this with theoretical expectations. In analogy to [32], I propose to call this breakdown "type 4."

VI. Conclusion

In the last 20 years, decisive progress has been made, to a good part by works done in our lab at MPI Halle, in understanding physical reasons for locally inhomogeneous dark currents in silicon solar cells. In this contribution, the origins of locally increased J_{01}-type, J_{02}-type, and ohmic currents, as well as of prebreakdown mechanisms are reviewed. By applying the DLIT-based "Local I-V" technique, the quantitative influence of such shunts on the cell efficiency can be estimated for different illumination intensities, which is exercised here for typical standard technology cells but can be done also for PERC cells [2], [3]. Also, prebreakdown phenomena in silicon solar cells are now widely understood. There are strong indications that the dominating prebreakdown mechanism in otherwise perfect monocrystalline Si solar cells is trap-assisted tunneling across surface states at the cell edge.

Acknowledgment

References

[1] Photovoltaics Report, Fraunhofer ISE, Freiburg, Germany, 2018. [Online]. Available: www.ise.fraunhofer.de

[2] P. P. Altermatt *et al.*, "High-performance p-type multcrystalline silicon (ms-Si): Its characterization and projected performance in PERC cells," *Sol. Energy*, 2018. [Online]. Available: https://doi.org/10.1016/j.solener.2018.01.073

[3] O. Breitenstein, F. Frühauf, and J. Bauer, "Advanced local characterization of silicon solar cells," *Physica Status Solidi a*, vol. 24, 2017, Art. no. 170061, doi: 10.1002/pssa.201700611.

[4] M. Padilla, B. Michl, B. Thaidigsmann, W. Warta, and M. C. Schubert, "Short-circuit current density mapping for solar cells," *Sol. Energy Mater. Sol. Cells*, vol. 120, pp. 282–288, 2014.

[5] P. Basore, "Extended spectral analysis of internal quantum efficiency," in *Proc. 23rd IEEE Photovolt. Spec. Conf.*, 1994, pp. 147–152.

[6] 2018. [Online]. Available: www.pv-tools.de and http://tauscience.com/flashqe-1

[7] O. Breitenstein, W. Warta, and M. Langenkamp, *Lock-in Thermography*, 2nd ed. Heidelberg, Germany: Springer, 2010.

[8] O. Breitenstein, "Nondestructive local analysis of current-voltage characteristics of solar cells by lock-in thermography," *Sol. Energy Mater. Sol. Cells*, vol. 95, pp. 2933–2936, 2011.

[9] 2018. [Online]. Available: http://www.maxplanckinnovation.com/en/

[10] O. Breitenstein, F. Frühauf, and M. Turek, "Improved empirical method for calculating short circuit current density images of silicon solar cells from saturation current density images and vice versa," *Sol. Energy Mater. Sol. Cells*, vol. 154, pp. 99–103, 2016.

[11] K. Ramspeck *et al.*, "Recombination current and series resistance imaging of solar cells by combined luminescence and lock-in thermography," *Appl. Phys. Lett.*, vol. 90, 2007, Art. no. 153502.

[12] O. Breitenstein, "Local efficiency analysis of solar cells based on lock-in thermography," *Sol. Energy Mater. Sol. Cells*, vol. 107, pp. 381–389, 2012.

[13] K. Bothe and D. Hinken, "Quantitative luminescence characterization of crystalline silicon solar cells," in *Advances in Photovoltaics*, vol. 2. Burlington, NJ, USA: Academic, 2013.

[14] M. Schneemann, T. Kirchartz, R. Carius, and U. Rau, "Measurement and modeling of reverse biased electroluminescence in multi-crystalline silicon solar cells," *J. Appl. Phys.*, vol. 114, 2013, Art. no. 134509.

[15] T. Trupke, E. Pink, R.A. Bardos, and M.D. Abbott, "Spatially resolved series resistance of silicon solar cells obtained from luminescence imaging," *Appl. Phys. Lett.*, vol. 90, 2007, Art. no. 093506.

[16] O. Breitenstein, J. Bauer, D. Hinken, and K. Bothe, "The realibility of thermography- and luminescence-based series resistance and saturation current density imaging," *Sol. Energy Mater. Sol. Cells*, vol. 137, pp. 50–60, 2015.

[17] D. Macdonald and A. Cuevas, "Reduced fill factors in multicrystalline silicon solar cells due to injection-level dependent bulk lifetimes," *Prog. Photovolt., Res. Appl.*, vol. 8, pp. 363–375, 2000.

[18] O. Breitenstein, "Understanding the current-voltage characteristics of industrial crystalline silicon solar cells by considering inhomogeneous current distributions," *Opto-Electron. Rev.*, vol. 21, pp. 259–282, 2013.

[19] J. Bauer *et al.*, "Recombination at Lomer dislocations in multicrystalline silicon for solar cells," *IEEE J. Photovolt.*, vol. 6, no. 1, pp. 100–110, Jan. 2016.

[20] A. Bourret, J. Desseaux, and A. Renault, "Core structure of the Lomer dislocation in germanium and silicon," *Philosoph. Mag. A*, vol. 45, pp. 1–20, 1982.

[21] O. Breitenstein and J. Heydenreich, "Non-ideal I-V characteristics of block-cast silicon solar cells," *Solid-State Phenomena*, vol. 37/38, pp. 139–144, 1994.

[22] O. Breitenstein *et al.*, "Interpretation of the commonly observed I-V characteristics of c-Si cells having ideality factors larger than 2," in *Proc. 4th World Conf. Photovolt. Energy Convers.*, 2006, pp. 879–884.

[23] S. Steingrube *et al.*, "Explanation of commonly observed shunt currents in c-Si solar cells by means of recombination statistics beyond the Shockley-Read-Hall approximation," *J. Appl. Phys.*, vol. 110, 2011, Art. no. 014515.

[24] O. Breitenstein, J. P. Rakotoniaina, H. H. Al Rifai, and M. Werner, "Shunt types in crystalline silicon solar cells," *Prog. Photovolt., Res. Appl.*, vol. 12, pp. 529–538, 2004.

[25] N.F. Mott, *Metal-Insulator Transitions*. London, U.K.: Taylor & Francis, 1990.

[26] D. Lausch *et al.*, "Potential-induced degradation (PID): Introduction of a novel test approach and explanation of increased depletion region recombination," *IEEE J. Photovolt.*, vol. 4, no. 3, pp. 834–840, May 2014.

[27] S. Richter, J. Bauer, and O. Breitenstein, "Growth of carbon and nitrogen containing precipitates in crystalline solar silicon and their influence on solar cells," *Phys. Status Solidi RRL*, vol. 11, 2017, Art. no. 1600354.

[28] J. Bauer, O. Breitenstein, and J.P. Rakotoniaina, "Electronic activity of SiC precipitates in multicrystalline solar silicon," *Phys. Status Solidi*, vol. 7, pp. 2190–2195, 2007.

[29] F. Frühauf and O. Breitenstein, "DLIT- versus ILIT-based efficiency imaging of solar cells," *Sol. Energy Mater. Sol. Cells*, vol. 169, pp. 195–202, 2017.

[30] S.M. Sze and K.K. Ng, *Physics of Semiconductor Devices*. Hoboken, NJ, USA: Wiley, 2007.

[31] S.M. Sze and G. Gibbons, "Effect of junction curvature on breakdown voltage in semiconductors," *Solid-State Electron.*, vol. 9, pp. 831–845, 1966.

[32] O. Breitenstein *et al.*, "Understanding junction breakdown in multicrystalline solar cells," *J. Appl. Phys.*, vol. 109, 2011, Art. no. 071101.

[33] D. Lausch *et al.*, "Identification of pre-breakdown mechanism of silicon solar cells at low reverse voltages," *Appl. Phys. Lett.*, vol. 97, 2010, Art. no. 073506.

[34] M. Schneemann, A. Helbig, T. Kircharz, R. Carius, and U. Rau, "Reverse biased electroluminescence spectroscopy of crystalline silicon solar cells with high spatial resolution," *Phys. Status Solidi A*, vol. 207, pp. 2597–2600, 2010.

[35] A. Hähnel *et al.*, "Electron microscope verification of prebreakdown-inducing α-FeSi$_2$ needles in multicrystalline silicon solar cells," *J. Appl. Phys.*, vol. 113, 2013, Art. no. 044505.

[36] J. Bauer *et al.*, "Hot spots in multicrystalline silicon solar cells: Avalanche breakdown due to etch pits," *Phys. Status Solidi RRL*, vol. 3, pp. 40–42, 2009.

[37] O. Breitenstein, J. Bauer, J.-M. Wagner, and A. Lotnyk, "Imaging physical parameters of pre-breakdown sites by lock-in thermography techniques," *Prog. Photovolt., Res. Appl.*, vol. 16, pp. 679–685, 2008.

[38] J. Bauer, D. Lausch, H. Blumtritt, N. Zakharov, and O. Breitenstein, "Avalanche breakdown in multicrystalline solar cells due to preferred phosphorous diffusion at extended defects," *Prog. Photovolt., Res. Appl.*, vol. 21, pp. 1444–1453, 2013.

Author photograph and biography not available at the time of publication.